

Magnetic fields and uniformity of radio frequency power deposition in low-frequency inductively coupled plasmas with crossed internal oscillating currents

E. L. Tsakadze, K. Ostrikov, Z. L. Tsakadze, S. V. Vladimirov, and S. Xu

Citation: [Physics of Plasmas](#) **11**, 3915 (2004); doi: 10.1063/1.1768176

View online: <http://dx.doi.org/10.1063/1.1768176>

View Table of Contents: <http://scitation.aip.org/content/aip/journal/pop/11/8?ver=pdfcov>

Published by the [AIP Publishing](#)

Articles you may be interested in

[Modulations of the plasma uniformity by low frequency sources in a large-area dual frequency inductively coupled plasma based on fluid simulations](#)

[Phys. Plasmas](#) **22**, 053508 (2015); 10.1063/1.4921670

[Effect of dual frequency on the plasma characteristics in an internal linear inductively coupled plasma source](#)

[Appl. Phys. Lett.](#) **89**, 251501 (2006); 10.1063/1.2405417

[Generation of uniform plasmas by crossed internal oscillating current sheets: Key concepts and experimental verification](#)

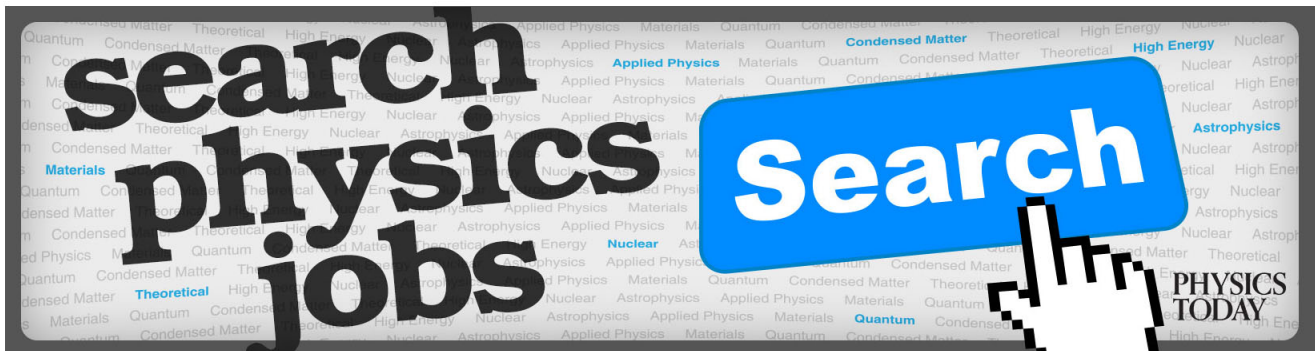
[J. Appl. Phys.](#) **97**, 013301 (2005); 10.1063/1.1826214

[Wave phenomena, hot electrons, and enhanced plasma production in a helicon discharge in a converging magnetic field](#)

[Phys. Plasmas](#) **11**, 3888 (2004); 10.1063/1.1764830

[Novel low-frequency oscillation in a radio-frequency inductively coupled plasma with tuned substrate](#)

[Phys. Plasmas](#) **11**, 3270 (2004); 10.1063/1.1740772



Magnetic fields and uniformity of radio frequency power deposition in low-frequency inductively coupled plasmas with crossed internal oscillating currents

E. L. Tsakadze

*Plasma Sources and Applications Center, NIE, Nanyang Technological University, 1 Nanyang Walk, 637616 Singapore, Singapore
and Optics and Plasma Research Department, RISØ National Laboratory, P.O. Box 49, DK-4000 Roskilde, Denmark*

K. Ostrikov^{a)}

*School of Physics, The University of Sydney, New South Wales 2006, Australia
and Plasma Sources and Applications Center, NIE, Nanyang Technological University, 1 Nanyang Walk, 637616 Singapore, Singapore*

Z. L. Tsakadze

Plasma Sources and Applications Center, NIE, Nanyang Technological University, 1 Nanyang Walk, 637616 Singapore, Singapore

S. V. Vladimirov

School of Physics, The University of Sydney, New South Wales 2006, Australia

S. Xu^{b)}

Plasma Sources and Applications Center, NIE, Nanyang Technological University, 1 Nanyang Walk, 637616 Singapore, Singapore

(Received 17 February 2004; accepted 10 May 2004; published online 9 July 2004)

Radial and axial distributions of magnetic fields in a low-frequency (~ 460 kHz) inductively coupled plasma source with two internal crossed planar rf current sheets are reported. The internal antenna configuration comprises two orthogonal sets of eight alternately reconnected parallel and equidistant copper litz wires in quartz enclosures and generates three magnetic (H_z , H_r , and H_ϕ) and two electric (E_ϕ and E_r) field components at the fundamental frequency. The measurements have been performed in rarefied and dense plasmas generated in the electrostatic (E) and electromagnetic (H) discharge modes using two miniature magnetic probes. It is shown that the radial uniformity and depth of the rf power deposition can be improved as compared with conventional sources of inductively coupled plasmas with external flat spiral ("pancake") antennas. Relatively deeper rf power deposition in the plasma source results in more uniform profiles of the optical emission intensity, which indicates on the improvement of the plasma uniformity over large chamber volumes. The results of the numerical modeling of the radial magnetic field profiles are found in a reasonable agreement with the experimental data. © 2004 American Institute of Physics. [DOI: 10.1063/1.1768176]

I. INTRODUCTION

High-density, low-temperature rf plasma sources have been increasingly attractive for numerous industrial applications ranging from traditional highly selective dry etching and microstructuring of silicon wafers in ultra-large-scale integration semiconductor manufacturing to recently reported synthesis of carbon-based nanostructures in the fabrication of electron field emitters for the development of advanced flat display panels.^{1–4} High number density and excellent uniformity of fluxes of reactive species over large volumes and surface areas are crucial for the improvement of the efficiency of plasma processing. Among various rf plasma sources, inductively coupled plasma (ICP) devices have at-

tracted a great deal of attention because of their excellent properties to generate high-density, large-volume, and large-area plasmas. Presently, low-pressure, low-temperature ICP sources are used by several industries as reference plasma reactors for numerous applications in semiconductor manufacturing, optoelectronics, and synthesis and processing of advanced functional films and coatings.^{5,6}

The configurations and positioning of rf current driving antennas can be quite different. For example, the inductive coil can be either placed externally or internally with respect to the discharge chamber. In one of the most common embodiments, the inductively coupled plasma is sustained by the rf power deposited by an external flat spiral inductive coil ("pancake coil") installed externally to and separated by a small air gap from a dielectric window that seals a (usually cylindrical) vacuum chamber.^{7–9} Most of the commercial ICP reactors feature a fused silica or reinforced glass window

^{a)}Electronic address: K.Ostrikov@physics.usyd.edu.au

^{b)}Author to whom correspondence should be addressed. Electronic mail: syxu@nie.edu.sg

sealing the chamber in its r - ϕ cross section from the top. The rf current driven through the flat spiral inductive coil generates the electromagnetic field that features the azimuthal electric E_ϕ as well as the radial H_r and axial H_z magnetic field components.¹⁰

Due to the obvious symmetry of the problem, the azimuthal electric field features a dip near the chamber axis $r=0$. In the idealized case of concentric purely azimuthal rf currents $E_\phi(r=0)=0$.¹¹ This feature has been confirmed by the extensive magnetic probe measurements and numerical modeling results.^{11–15} Using the linear, with respect to the rf field amplitude, approximation, which is normally valid at low rf input powers,^{16–18} it was shown that the rf power deposition to the plasma is strongly nonuniform and the actual rf power density has a well-resolved minimum near the chamber axis.¹⁹ Representative contour plots of the rf power density in conventional sources of inductively coupled plasmas are shown in Figs. 7(b,d) of Ref. 19. This is consistent with the power density profiles derived through the mapping of the electromagnetic fields in the chamber and the results of optical emission spectroscopy.^{11,20,21} Thus, the improvement of the uniformity of the rf power deposition is one of the key concerns of modern plasma processing applications and several attempts to modify the inductive coil configuration and/or adjust the rf power coupling have been reported.^{22,23}

Recently, we have reported on the development of a source of low-frequency (~ 460 kHz) inductively coupled plasmas employing two orthogonal sets of eight rf currents reconnected alternately and driven inside the modified vacuum chamber.²⁴ According to the earlier theoretical predictions,¹⁹ we expect that the new antenna configuration will generate more uniformly distributed electromagnetic field patterns and will thus improve the uniformity of the rf power deposition. Here, we report on the experimental verification of this power deposition concept by the measurements of the distributions of the magnetic field and optical emission intensity of the selected argon species in the plasma source. We also show that the radial profiles of the rf magnetic fields and the contours of the rf power deposition are in a remarkable agreement with the numerical results.

The paper is organized as follows. In Sec. II, the details of the vacuum system, gas handling, rf input, antenna configuration, and magnetic probe design are given. The results of the experimental mapping of the magnetic field topography in the plasma source are presented in Sec. III. In Sec. IV, the experimental results from two different ICP sources are discussed and compared with the results of numerical computations. The paper concludes with the summary of the major results obtained and a brief outlook for the future research.

II. EXPERIMENTAL DETAILS

A simplified drawing of the low-frequency source of inductively coupled plasma, with the coordinates used, is given in Fig. 1. A vacuum vessel is a double-walled, water-chilled stainless steel chamber, with the inner radius of $R=16$ cm and length of $L=23$ cm. A semidome shaped top with the

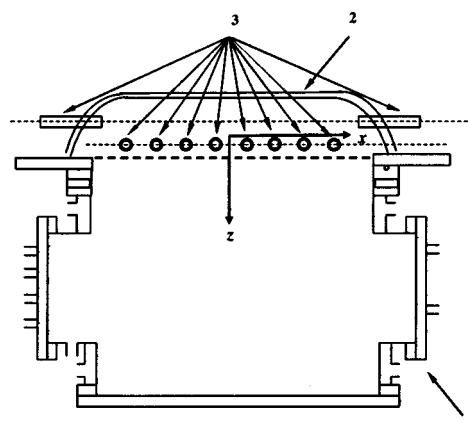


FIG. 1. Schematics of the plasma source with the internal antenna configuration: (1) vacuum chamber, (2) chamber top, (3) openings for the internal wires.

equidistantly positioned openings in the sidewalls seals off the vacuum chamber. Four rectangular side ports enable the access of various diagnostic tools or visual discharge observation. Two adjacent ports are positioned 90° apart and are equipped with seven axially aligned portholes for the Langmuir, optical emission, and magnetic probes.

The antenna comprises the two mutually orthogonal sets of parallel copper litz wires enclosed in cylindrical quartz tubes and introduced into the chamber top section through equidistantly positioned cylindrical openings as schematically shown in Fig. 2. The wires are reconnected in the way that the effective antenna impedance is reduced to the minimum, which is advantageous for the improvement of the rf power transfer efficiency.^{8,9} The antenna is powered by Advanced Energy PDX8000 0.46 MHz rf generator with the output range of 10–8000 W. The connection points are denoted by I and II, respectively. The generator is connected to the coil via an in-house designed π -type matching network. Since the total length of the antenna is much smaller than the electromagnetic wavelength at 460 kHz, it is reasonable to assume that the rf current has the same phase in all parts of the coil. Hence, the electric field with the two, radial E_r and

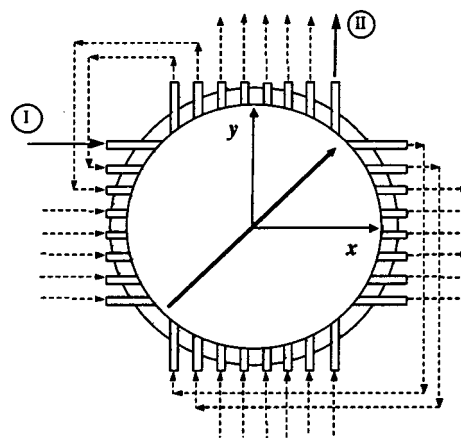


FIG. 2. The way of the current-carrying wire reconnection in the internal antenna with the minimized impedance. I and II denote the connection points of the rf generator. The bold solid arrowed line shows the direction of the generated electric field with the E_ϕ and E_r components. Reconnection of only four wires (two in each direction) is shown.

azimuthal E_ϕ , components, and the resulting direction as denoted by a bold solid arrowed line in Fig. 2 is excited. The arrow in Fig. 2 points at one of the side ports equipped with the diagnostic portholes. This direction will be further referred as $\phi=0^\circ$. The second side port with the portholes is located in 90° clockwise, and the corresponding azimuthal position is referred to as $\phi=90^\circ$. The bottom of the chamber also contained 16 portholes aligned radially at the azimuthal position $\phi=0^\circ$. Further details of the chamber and antenna configuration design and operation can be found elsewhere.²⁴

A combination of a 450 ls^{-1} turbo-molecular pump backed by a two-stage rotary pump allows one to achieve base pressures of the order of 10^{-5} Torr. The feedstock gas inlet and operating pressure can be controlled by MKS mass flow controllers. In this work, the argon gas pressure p_0 was maintained in the range of 20–100 mTorr. However, the plasma source is capable for stable work within the pressure range of 0.001–1 Torr,²⁴ which is suitable for most of the low-to-intermediate pressure plasma processing applications.^{25,26}

The distribution of the rf magnetic fields excited by the internal antenna configuration of Fig. 2 was measured using two miniature magnetic probes. The schematics and details of the magnetic probe design and operation can be found elsewhere.¹⁵ Briefly, the probes are made of 5 mm thick cylindrical Teflon heads mounted on thinner hollow aluminum tubes. Two miniature solenoids made of thin insulated copper wires are wound around the Teflon heads as shown in Fig. 2 of Ref. 15. Depending on the orientation of the solenoids, the magnetic probes can sense either the radial magnetic field component H_r (“radial probe”) or H_ϕ/H_z components (two different positions of the “azimuthal/axial” probe). To map the spatial distribution of the magnetic fields in the chamber, the probes have been inserted radially or axially through the portholes in the diagnostic side ports (at $\phi=0^\circ$ and $\phi=90^\circ$) and bottom plate of the chamber.

The mapping of the magnetic field distribution was complemented by the measurements of the radial and axial profiles of the optical emission intensity of selected spectral lines of argon atoms and singly ionized ions in the wavelength range of 300–900 nm. The optical emission of different spectral lines of the excited/ionized species produced by the plasma discharge was collected by a collimated optical probe inserted radially or axially into the plasma chamber. An optical fiber was used to transmit the collected signal to the entrance slit of a monochromator (Acton Research SpectraPro-750i model, 0.750 Meter Focal Length Triple Grating Imaging Monochromator/Spectrograph). The emission amplified by a THORN EMI photomultiplier was dispersed and analyzed by the above monochromator, which had a spectral resolution of 0.023 nm. In order to monitor the output signal on the computer in real time, the signal was continuously digitized by an analog to digital convertor built-in in the scan controller. The scanning and data acquisition process was controlled by the data acquisition and analysis software SPECTRASENSE™ (Acton Research Corporation). Using the data acquisition system, we were able to record broad spectral bands or selectively monitor certain spectral lines.

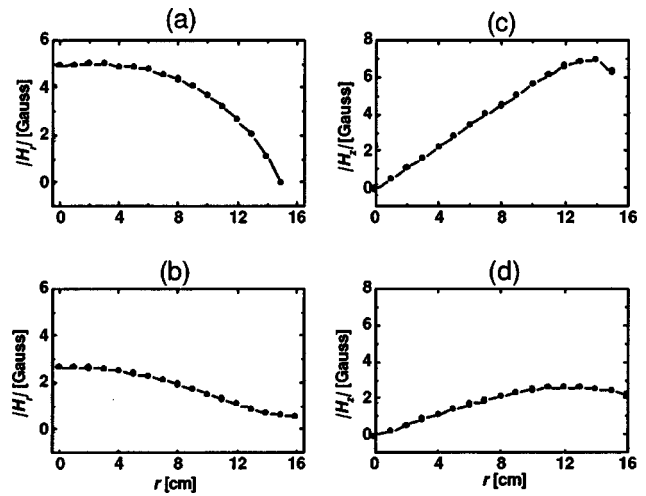


FIG. 3. Radial distribution of the amplitude of the induced radial (a), (b) and axial (c), (d) components of the magnetic field in the plasma chamber fully filled by the rarefied plasma ($n_{e,i}=3.3\times 10^9\text{ cm}^{-3}$). Argon gas pressure p_0 and the total power deposited into the plasma P_p are 30 mTorr and 300 W, respectively. Measurements are performed at the axial positions $z=8$ (a), (c) and $z=14$ cm (b), (d) and azimuthal angle $\phi=90^\circ$.

III. EXPERIMENTAL RESULTS

The measurements of the magnetic field topography in the chamber have been conducted in three different regimes, namely, in a fully evacuated chamber, in low-, and high-density plasmas. The low-density (rarefied) plasma, with the spatially averaged electron/ion number densities $n_{e,i}\sim 3.3\times 10^9\text{ cm}^{-3}$ was generated in the low-input-power (~ 300 W) electrostatic (E) discharge mode at 30 mTorr. On the other hand, the high-density ($n_{e,i}\sim 6\times 10^{11}\text{ cm}^{-3}$) plasma was sustained with 770 W rf powers in the electromagnetic (H) mode of the discharge at the same gas feedstock pressure. The electron/ion densities were measured using a conventional Dryvestein's routine without assumption of any specific electron energy distribution function.²⁵

Below, we will show that the magnetic field measurements complemented by simple relations between the field components following from Maxwellian equations confirm that the actual electromagnetic field excited by the antenna configuration of our interest here indeed features two components of the electric field E_ϕ and E_r , and three components of magnetic field H_z , H_r , and H_ϕ (TE electromagnetic field²⁷), in a remarkable agreement with earlier numerical predictions.¹⁹

First, we have observed that the difference between the magnetic field values and distributions in the evacuated and rarefied plasma cases is minor and the corresponding deviations typically do not exceed a few percent. For this reason, here we present the results in the low- and high-density plasma cases only. Figures 3 and 4 display the radial profiles of the magnetic field amplitudes measured at different axial and azimuthal positions in the E -mode discharge. Specifically, Fig. 3 shows the radial distributions of H_r and H_z at $\phi=90^\circ$ and two axial positions, namely, $z=8$ and $z=14$ cm from the midplane between the two sets of mutually perpendicular coils (the beginning of the Cartesian coordi-

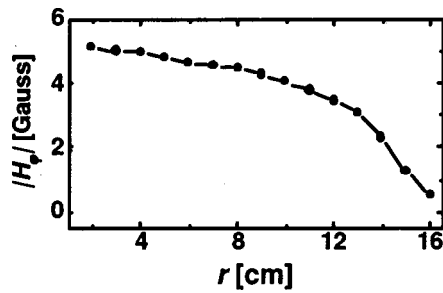


FIG. 4. Radial distribution of the amplitude of the induced azimuthal component of the magnetic field in the rarefied plasma for the axial position $z = 8$ cm and azimuthal angle $\phi = 0^\circ$. Other parameters are the same as in Fig. 3.

nate system in Fig. 1). It was also noted that the phase of the rf magnetic field is almost constant (with respect to the phase of the rf current), and is not shown here. In particular, Fig. 3 demonstrates the penetration of the radial and azimuthal magnetic field in the low-density E -mode plasma. In this case the character of the field penetration is weakly reflected by the expected evanescence due to the “skin effect,” characterized by the penetration length in the plasma,

$$l_s \approx [Y^2 - (\omega/c)\varepsilon(n_{e,i})]^{1/2}, \quad (1)$$

where $Y = \rho_1/R$, ρ_1 is the first root of the first derivative of the Bessel function of the first kind, and ω is the frequency of the electromagnetic field.¹⁹ The results of Fig. 3 suggest that the amplitude of the radial magnetic field component peaks near the chamber axis, slowly decreases along the radius, and vanishes thereafter in the vicinity of the walls. Meanwhile, one can see that the amplitude of the axial component of the induced magnetic field has a zero value at $r = 0$ and a clear maximum at $r = 12$ – 14 cm (depending on the axial position) from the center. This is in a good agreement with the boundary conditions suggesting that the tangential component of the electric field and normal component of the magnetic field have to vanish at the sidewalls of the chamber.²⁷

The azimuthal magnetic field H_ϕ is 90° azimuthally phase shifted with respect to H_r and H_z and its radial distribution was measured at the axial position $z = 8$ cm (Fig. 4).

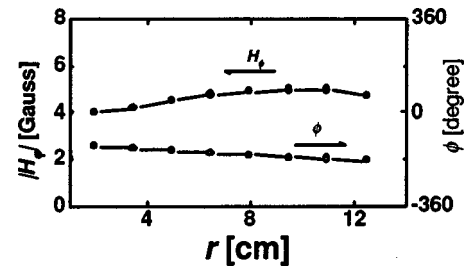


FIG. 6. Radial distribution of the amplitude (solid circles) and phase (void circles) of the induced azimuthal component of the magnetic field in the H -mode discharge, for the same parameters as in Fig. 5. Measurements are made at the axial position $z = 8$ cm and azimuthal angle $\phi = 0^\circ$.

This component is not present in the linear electromagnetic field pattern of the conventional ICP source with a planar spiral coil and can appear as a result of the nonlinear Lorentz force action at elevated rf power inputs.¹⁵ From Fig. 4, it is evident that the amplitude of H_ϕ is fairly uniform (as compared with the radial and azimuthal magnetic fields) within the radial distances $r = 0$ – 10 cm, peaks at $r = 0$ and slowly diminishes towards the walls, which is also consistent with the numerical results.¹⁹

Figures 5 and 6 show the radial distributions of H_r , H_z , (Fig. 5), and H_ϕ (Fig. 6) components in the H -mode discharge in argon sustained with 770 W input powers at 30 mTorr. The Langmuir probe measurements suggest that the spatially averaged values of the plasma density and effective electron temperature are $n_{e,i} = 6 \times 10^{11} \text{ cm}^{-3}$ and $T_{\text{eff}} = 3.2 \text{ eV}$, respectively. Apparently, at higher plasma densities the effect of screening of the electromagnetic field by the plasma becomes more pronounced, which certainly affects the field topography in the chamber. Generally speaking, an increase of the plasma density results in the three main changes of the field patterns. First, the amplitudes of the induced magnetic fields become smaller at the same axial position. Second, the signal phase variations along the radius become more pronounced. Third, the character of the radial variation of some components becomes quite different from the low-density plasma case. From Figs. 5 and 6 one can see that the most apparent changes happen to the radial magnetic

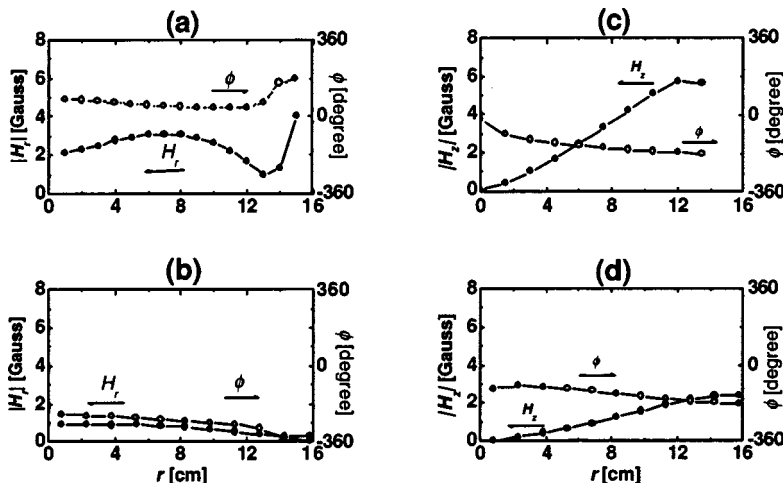


FIG. 5. Radial profiles of the amplitude (solid circles) and phase (void circles) of the induced radial (a), (b) and azimuthal (c), (d) components of the magnetic field in the chamber filled by dense ($6 \times 10^{11} \text{ cm}^{-3}$) plasma for $z = 8$ (a), (c) and 12 cm (b), (d). Total input power into the plasma is $P_p \sim 770 \text{ W}$. Other parameters are the same as in Fig. 3.

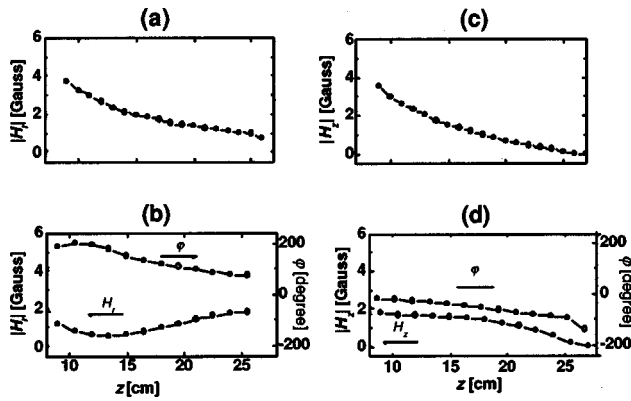


FIG. 7. Axial profiles of the amplitude (solid circles) and phase (void circles) of H_r (a), (b) and H_z (c), (d) magnetic field components in the rarefied (a), (c) and dense (b), (d) argon plasma. Measurements are performed at the radial position $r=8$ cm and azimuthal angle $\phi=90^\circ$. Parameters of the rarefied (a), (c) and dense (b), (d) plasmas are the same as in Figs. 3 and 5, respectively.

field component, whereas the effect of the plasma density on H_z appears to be the weakest.

Figures 7 and 8 display the axial profiles of the induced magnetic field components. The measurements were performed by inserting the magnetic probes through the quartz feedthroughs inserted through the holes in the bottom endplate of the chamber and aligned parallel to the chamber axis. The radial and axial components were measured at the radial position $r=8$ cm and azimuthal angle $\phi=90^\circ$, while the H_ϕ component was measured on the chamber axis $r=0$ and $\phi=0^\circ$. The choice of the radial position to measure the signal was motivated by the relative maxima in the radial profiles in the corresponding magnetic field components. We recall that the azimuthal angle ϕ was measured with respect to the direction of the resulting oscillating rf current and the

axial coordinate with respect to the midplane between the parallel current sheets as shown in Fig. 1.

From Figs. 7(a,c) and 8(a) one can note that in the electrostatic discharge mode all three components show a consistent tendency to decrease away from the excitation source. It is also remarkable that the amplitudes of all three components decrease in approximately four times when the probe was moved downwards from $z=9$ to $z=25$ cm. From Fig. 7(c) we can also see that the axial magnetic field vanishes at the bottom endplate of the chamber, in accordance with the required boundary conditions.²⁷

Switching the discharge to the electromagnetic (H) mode results in remarkable changes in the distribution of the electromagnetic field in the plasma chamber. First, the amplitudes of all three components are smaller near the internal antenna as compared with the rarefied plasma case. Second, the decaying profile of the axial magnetic field component [Fig. 7(d)] becomes smoother and more uniform compared to the corresponding profile [Fig. 7(c)] in the E -mode discharge. Third, the character of variation of H_r and H_ϕ components with z changes dramatically. Indeed, the initial relatively smooth decay changes to the rise at $\approx z=14-15$ cm. We emphasize that the observed rise of the amplitudes of magnetic fields while approaching the bottom endplate is not common for conventional sources of inductively coupled plasmas. The experimental mapping of the magnetic field profiles in the cylindrical discharge vessel has thus confirmed that the enhanced, as compared to conventional sources of low-frequency inductively coupled plasmas,¹³ penetration of the electromagnetic field into the chamber can be achieved by introducing a new internal rf antenna that comprises the two internal oscillating current sheets and generates all three components of magnetic field H_r , H_z , and H_ϕ , in accordance with earlier theoretical predictions and numerical results.¹⁹

IV. DISCUSSION

From the arrangement of the internal coil one can easily conclude that the electric field generated by the antenna oscillates in the $r-\phi$ plane in the direction of the bold solid arrowed line in Fig. 2. Thus, the electromagnetic field does not feature an axial electric field E_z component, which is consistent with the coil arrangement and the symmetry of the problem. Apparently, the rf current inductively driven inside the chamber also oscillates in the same ($r-\phi$) direction. However, since the currents have to form closed loops, it is reasonable to presume that the return path for this current goes through the $r-z$ ("poloidal") cross section. Therefore, this could be one of the major factors in the explanation of deeper penetration of the electromagnetic field inside the plasma as compared to the conventional ICP sources with flat spiral coils that generate (at low and moderate rf powers) purely azimuthal rf electric fields and currents, the latter having the return loops in the $r-\phi$ cross section. In the latter case, one can attribute the field penetration mostly to the skin effect that controls the electromagnetic field penetration into dense plasma media with the plasma frequency exceeding the frequency of the incident wave.²⁸ In our case, a combi-

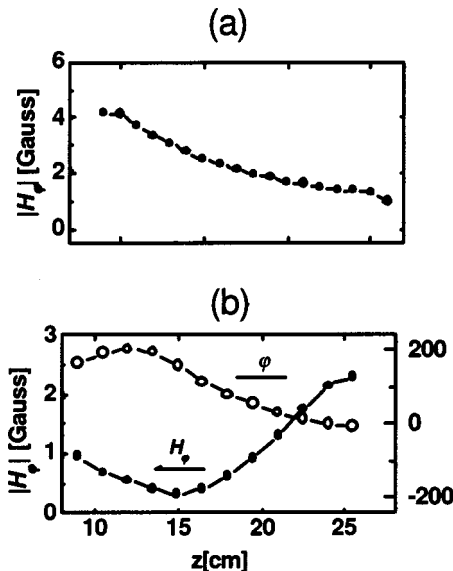


FIG. 8. Axial profiles of the amplitude (solid circles) and phase (void circles) of the induced azimuthal component of the magnetic field: (a) rarefied plasma, (b) dense plasma. Other parameters are the same as in Fig. 7.

nation of the two major factors, namely, the excitation of poloidal rf current loops and skin-effect results in a pronounced penetration of the electromagnetic field inside the vacuum chamber. A deep penetration of magnetic fields into the chamber has convincingly been confirmed by the results of magnetic field measurements presented in Figs. 3–8. It is also noteworthy that this phenomenon is also affected by nonzero values of the E_z component that might appear in a real discharge due to a finite gap (neglected in numerical calculations in Ref. 19) and hence, a potential difference between the two parallel current sheets in the coil.

In the above, we have not shown the spatial profiles of the induced magnetic fields in the fully evacuated plasma chamber. However, as we have mentioned above, such profiles are quite similar to the rarefied plasma case. It is thus interesting to estimate at what values of the plasma density the effects of the plasma screening of the electromagnetic fields come into play. We have estimated that by comparing the relative impacts of the geometric Y^2 and plasma screening $(\omega/c)\varepsilon^{1/2}$ terms in the expression for the skin length (1). The estimates show that the spatially averaged plasma density should exceed $n_{e,i} \sim 4 \times 10^9 \text{ cm}^{-3}$ for the classical plasma screening effects to become significant. In the case presented, the spatially averaged plasma density in the electrostatic (E) mode was $\approx 3.3 \times 10^9 \text{ cm}^{-3}$, which is below the estimated threshold.

When the plasma density was increased by more than two orders of magnitude (to $6 \times 10^{11} \text{ cm}^{-3}$) by switching the discharge to the high-density electromagnetic (H) mode, several remarkable changes in the spatial profiles of magnetic fields were observed. However, the relative changes in the radial profiles (Figs. 5 and 6) were not as pronounced as in the axial ones (Figs. 7 and 8). Furthermore, similar changes in the radial topography of magnetic fields are much stronger in conventional inductively coupled plasma sources with a planar external coil.¹³ In particular, as suggested by the results in Figs. 3 and 5, the amplitudes of H_r and H_ϕ components decrease in ≈ 1.5 –2 times at the same axial position. On the other hand, the axial magnetic field component was affected by the plasma density variations even to the less extent (Figs. 4 and 6). In a conventional ICP configuration with a flat spiral coil a similar change would be at least several times larger.^{14,19} One can attribute this observation to the relatively high importance (as compared with the ICP planar-coil sources) of the geometrical factor Y and the generation of poloidally circulating rf currents that maintain a strong azimuthal magnetic field, which is yet another distinctive feature of the antenna configuration of our interest here. From the axial profiles shown in Figs. 7 and 8 one can deduce a remarkable discrepancy with the conventional exponential evanescence predicted by the classical theory of the skin effect in the plasma. Specifically, the expected evanescence estimated by using the previous modeling results¹⁹ would be at least 20–25 times as compared to the actually recorded decline in a factor of 4–10.

We emphasize that the radial profiles (Figs. 5 and 6) in the electromagnetic discharge mode are quite different but generally reproduce similar trends in the rarefied plasmas. The axial profiles, on the contrary, show quite different be-

havior (Figs. 7 and 8). A possible explanation could be that the geometric factors control the radial magnetic field distribution, whereas the plasma eigenmodes are excited along the axial direction.

Another possibility is that similarly to conventional ICPs with external planar coils, the excitation of the azimuthal magnetic field H_ϕ can enhance the penetration of the rf field due to nonlinear effects,²⁹ which become stronger at lower frequencies of the rf generator.¹² However, since the azimuthal magnetic field component is generated at the fundamental frequency (as confirmed by the results in Figs. 3–8) we should expect that the enhanced penetration of the magnetic field can be achieved as a result of *primary* nonlinear effects. In conventional inductively coupled plasmas with external flat spiral coil the H_ϕ component does not appear at the fundamental frequency and the enhanced penetration of the magnetic field can be achieved as a result of *secondary* nonlinear effects only. This phenomenon warrants further experimental and modeling endeavors in the near future.

The operation of the plasma source in the high-density electromagnetic mode also affects the phase $\varphi_j = \arccot[\text{Re}(H_j)/\text{Im}(H_j)]$, which controls the relation between the real $\text{Re}(H_j)$ and imaginary $\text{Im}(H_j)$ parts of the j th component of the induced magnetic field. In the rarefied plasma, the field oscillations are almost synphased with the rf current [for this reason the phase is not shown in Figs. 3, 4, 7(a,c), and 8(a)] and $\text{Re}(H_j) \gg \text{Im}(H_j)$. When the plasma density increases, the imaginary parts of the magnetic fields become values of the same order of magnitude as the real parts, accompanied by a notable phase shift with respect to the antenna current.

To verify the experimental results, we have computed the radial profiles of the magnetic field components in the dense plasma case by using our earlier model of a spatially uniform plasma¹⁹ with the plasma density that equals to the spatially averaged electron/ion number density derived from the Langmuir probe measurements. The numerical results plotted as dashed curves in Fig. 9 generally reproduce the measured radial variations of the magnetic field and are also in a fairly good quantitative agreement with the experimental data. The apparent source of the remaining discrepancy between the theoretical and experimental results is the actual nonuniformity of the plasma in the chamber. The new models properly accounting the nonuniform distributions of the plasma density in the plasma source of interest here are eagerly anticipated in the near future. Meanwhile, various nonlinear effects, such as generation of the second (and higher) harmonic current, ponderomotive and Lorenz forces, become more important at higher power levels and can affect the field distribution in the chamber.^{15,30}

Furthermore, using the experimental map of the magnetic fields and the relations between the electric and magnetic fields following from the set of Maxwell's equations (see, e.g., Eqs. (2)–(8) of Ref. 19) we have obtained the distribution of the rf power deposited in the discharge chamber,

$$P_p = \frac{1}{2} \int_0^{2\pi} \int_0^R \int_0^L r \text{Re}(\sigma_p) |\mathbf{E}|^2 d\phi dr dz, \quad (2)$$

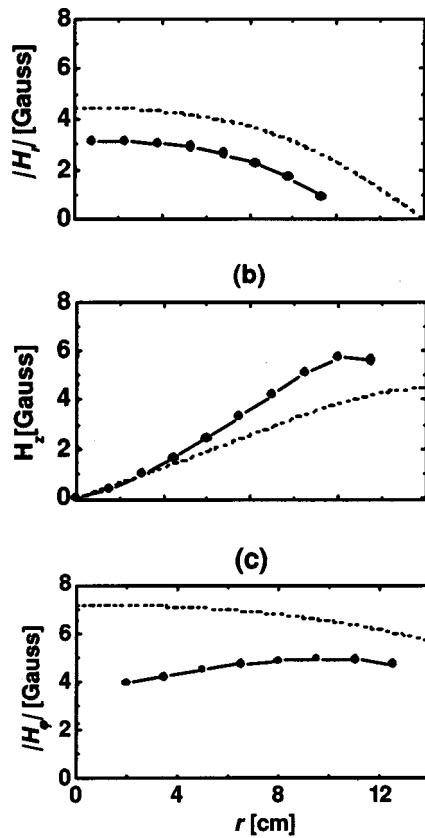


FIG. 9. Comparison of the measured (solid circles) and computed (dashed line) radial profiles of the magnetic field components in the H -mode discharge. Parameters are the same as in Fig. 5.

where

$$|\mathbf{E}|^2 = [\text{Re}(E_r)]^2 + [\text{Im}(E_r)]^2 + [\text{Re}(E_\phi)]^2 + [\text{Im}(E_\phi)]^2,$$

$\sigma_p = \omega_{pe}^2 / 4\pi(\nu_e - i\omega)$ is the conductivity of the uniform collisional plasma, ω_{pe} is the electron Langmuir frequency. Here, ν_e is the effective rate of electron collisions and ω is the frequency of the rf generator. A representative semiquantitative contour plot in Fig. 10 unambiguously confirms that the fairly uniform profiles of the rf power deposition have indeed been achieved experimentally. It is notable that the power density profiles shown in Fig. 10 favorably differ (especially in the areas adjacent to the chamber axis) from the

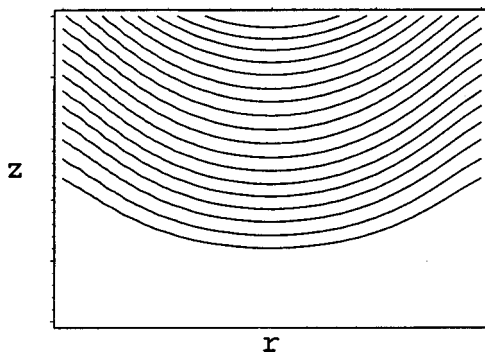


FIG. 10. Semiquantitative contour plot of the rf power density in the plasma source obtained from the experimental mapping of magnetic field distribution for the same parameters as in Fig. 5.

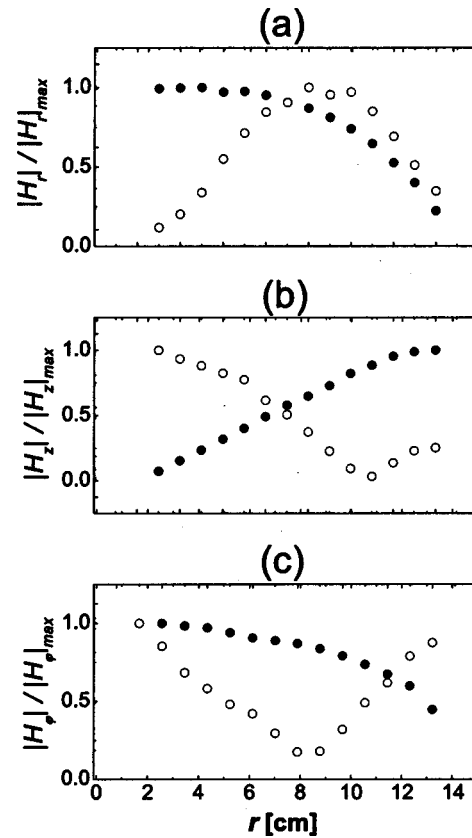


FIG. 11. Comparison of radial profiles of non-dimensional magnetic field components in the electrostatic (E) operation mode of the plasma sources with the internal (solid circles, parameters are the same as in Figs. 3 and 4) and external “pancake” (empty circles, rf input power of 170 W, gas pressure of 50.8 mTorr, and axial position $z = 4$ cm) rf coil configurations.

two-dimensional contour plots and three-dimensional profiles shown in Figs. 7(b,d) Ref. 19 and 9(b),¹⁹ respectively.

It is worthwhile to compare the spatial profiles of the rf magnetic fields in the plasma source of our interest here and conventional source of inductively coupled plasmas with the external flat spiral coil. Figures 11 and 12 show the radial profiles of the nondimensional H_z , H_r , and H_ϕ magnetic field components in both plasma sources in the electrostatic (E) and electromagnetic (H) modes, respectively. In all cases the ICP discharges were sustained in the same vacuum chamber and under fairly similar conditions. The difference was in the actual antenna configuration used. To plot the nondimensional profiles of the magnetic field components in the “conventional” ICP with the 17-turn flat spiral coil, the data of Refs. 13 and 15 were used. Each of the components was normalized on its maximum value over the radial span of the chamber, i.e., $\bar{H}_j(r) = H_j(r) / H_{j,\max}$, where $j = r, z, \phi$. Despite some difference in the discharge parameters, from Figs. 11 and 12 one can figure out the major differences in the rf field distributions in both plasma sources. To be more concise in the description, we will further refer to the conventional ICP sources with the flat external coil antenna configuration simply as the “ICP source” and to the new plasma source of our interest here as the plasma source with the internal oscillating current (PSIOC).

One can conclude from Figs. 11 and 12 that the magnetic

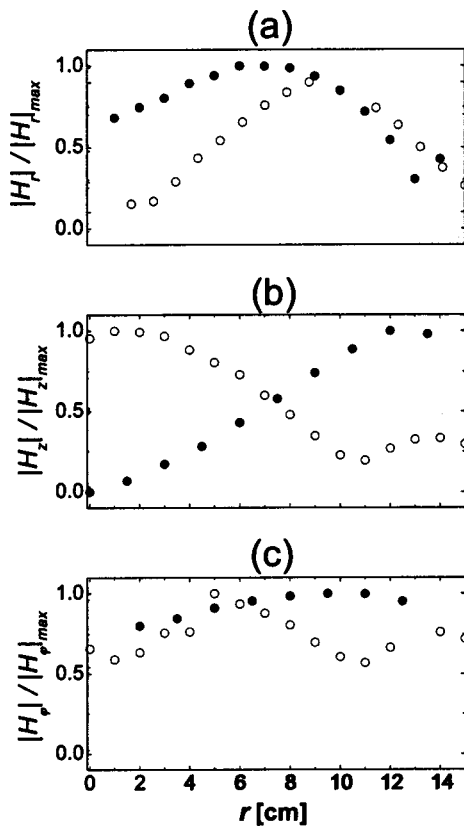


FIG. 12. Same as in Fig. 11 in the electromagnetic (H) discharge mode. For the solid data circles, parameters are the same as in Figs. 5 and 6. The empty circles correspond to the rf input power of 1130 W, and the same gas pressure and axial position as in Fig. 11.

field profiles are generally smoother in the PSIOC. It is also seen that different field components feature quite different behavior near the chamber axis. For instance, in the vicinity of $r=0$ the radial magnetic field component in the PSIOC is much larger than in the ICP. On the other hand, near the chamber axis, the H_z component is close to its peak value in the ICP and is very small in the PSIOC. From Figs. 11(c) and 12(c) one can conclude that the radial uniformity of the H_ϕ component is remarkably better in the PSIOC. Furthermore, the absolute value of the azimuthal magnetic field component (at the rf generator frequency) (Ref. 15) in the ICP is much smaller compared to all other magnetic field components in Figs. 11 and 12. The peak locations are also quite different in the two plasma devices. In the low-power E -mode discharge in the PSIOC, the H_r and H_ϕ components peak near the chamber axis, whereas the H_z component reaches its maximum at the chamber periphery. Meanwhile, in the H -mode discharge in the PSIOC, the maximum values of the H_r and H_z components shift to the plasma bulk ($r \sim 7-10$ cm). On the other hand, the H_r and H_z components show a similar peak behavior in both modes of the ICP discharge. The radial magnetic field component peaks at $r \sim 9-10$ cm, whereas the H_z component features a well-resolved minimum at $r \sim 10.5-11.5$ cm.

Using the data of Figs. 3–6, 11, and 12, as well of Fig. 3,¹⁵ we will now qualitatively relate the radial profiles of the magnetic field components to the uniformity of the rf power

deposition in both plasma sources. First, from Fig. 3 (Ref. 15) one can observe that $|H_r| \ll |H_z|$ near the chamber axis of the ICP source. However, at larger radii (e.g., at the mid-radius distance), the H_r component becomes much larger than H_z . Furthermore, $|H_{r,\max}| \sim 3|H_{z,\max}|$ and $|H_\phi| \ll |H_z|$, $|H_r|$.¹⁵ Hence, the quantity

$$\eta = \sqrt{|H_r|^2 + |H_z|^2 + |H_\phi|^2},$$

which is proportional to the rf power density in the chamber, does feature a dip within a few centimeters from the axis, which is consistent with the data shown in Figs. 7(b,d) (Ref. 19) and 9(b).¹⁹

Contrary to the ICP case, the amplitudes of all magnetic field components in the PSIOC remain within the same range at different radial positions. It is also remarkable that the variations of the azimuthal component are very slow (Figs. 4 and 6). Furthermore, a decrease of H_r with r is “balanced” by a similar increase of H_z . Therefore, the radial dependence of η should indeed follow the pattern shown in Fig. 10 and feature a somewhat better uniformity compared to the ICP case. Unfortunately, due to the difference in the operation parameters of our experiments here with the available earlier data,^{13,15} the actual improvement of the uniformity of the rf power deposition cannot be unambiguously quantified at this stage and the comparison under *identical* conditions is required in the near future. Likewise, the absence of the detailed axial scans of the magnetic fields in the ICP source^{13,15} disables a comprehensive comparison of the dependence $H_j(z)$ at different radii. However, we have recorded that the maximum amplitudes of the H_r component measured through the two adjacent upper portholes (separated by 4 cm) in the H -mode ICP discharge differ in at least three to four times, whereas a similar difference inferred from Fig. 5 does not exceed a few tens of percents. This certainly evidences a deeper penetration of the magnetic fields in the PSIOC as compared to the ICP.

Generally speaking, one should be cautious in relating the uniformity of the rf power deposition to the uniformity of the plasma density profiles and the fluxes of neutral/ion species onto the surface being processed. For example, in cylindrical plasma sources with the external helical coils, the rf power density peaks near the edge, whereas the plasma density is maximal near the chamber axis.²⁵ For this reason, only the direct mapping (e.g., by using rf-compensated single Langmuir probes) of the plasma density in both plasma sources can yield a conclusive answer on the actual improvement of the uniformity of the plasma density in the PSIOC compared with the ICP. The preliminary results²⁴ allow us to be quite optimistic in this regard and we expect to report the results in the near future.

A reasonable indication of the improvement of the uniformity of the plasma density in the PSIOC can be obtained from the results of direct comparison of the spatially resolved radial (Fig. 13) and axial (Fig. 14) profiles of the optical emission intensity (OEI) in the two plasma devices. In both figures, the OEIs of selected emission lines of neutral and ionized argon species are shown. Assuming the electron impact processes to be the main mechanisms responsible for the excitation of argon species, one obtains $\mathcal{I}_n^{\text{Ar}} \sim n_n n_e$ and

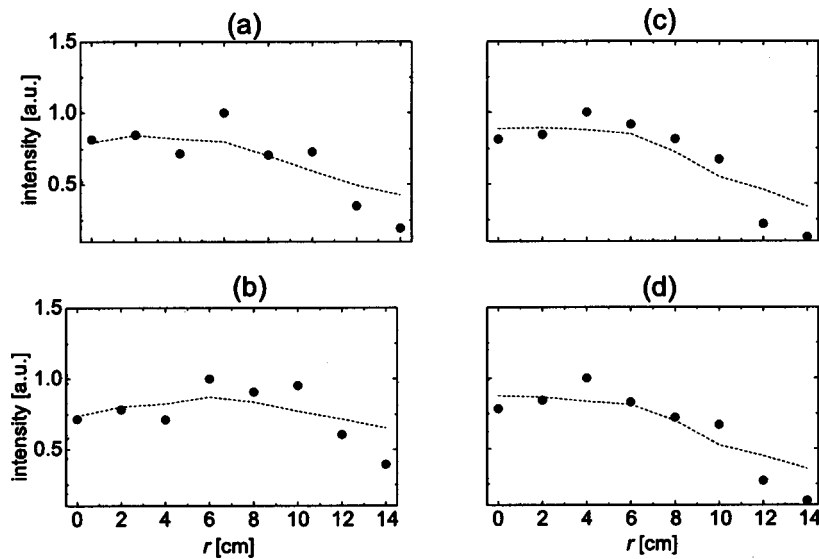


FIG. 13. Comparison of nondimensional radial profiles of the OEI of selected optical emission lines from the H -mode discharges in the plasma sources with the internal (a), (b) [$P_p \sim 640$ W, $p_0 = 51$ mTorr, and $\phi = 0^\circ$] and external “pancake” (c), (d) [$P_p \sim 670$ W, $p_0 = 29$ mTorr (Ref. 21)] rf coil configurations. Diagrams (a) and (c) correspond to 840.82 and 420.07 nm spectral lines of argon atoms, respectively. Diagrams (b) and (d) correspond to 386.9 and 434.81 nm emission lines of singly ionized argon ions, respectively.

$\mathcal{I}_i^{\text{Ar}} \sim n_i n_e$, where $\mathcal{I}_n^{\text{Ar}}$ and $\mathcal{I}_i^{\text{Ar}}$ are the optical emission intensities of the neutral and singly ionized argon species, and n_n is the number density of the argon neutrals. In the vacuum chamber used in both devices, the distribution of the neutral species can be considered uniform due to the uniform “showerlike” gas inlet through multiple orifices in the upper flange of the chamber.¹³ Hence, the radial and axial profiles of $\mathcal{I}_n^{\text{Ar}}$ in Figs. 13(a,c) and 14(a,c) fairly accurately reflect the distribution of the electron number density (and, hence, n_i due to the overall charge neutrality) in the reactor chamber. To this end, it is clear that the axial uniformity of the plasma density [Figs. 14(a,c)] is indeed better in the PSIOC. The profiles of the OEI of argon ions [which reflect the distribution of the product $n_i(r,z)n_e(r,z)$] also show very similar tendencies, with the expected faster decline of $\mathcal{I}_i^{\text{Ar}}$ with z [Fig. 14(d)]. From the results and discussions above, we can attribute the observed axial profiles of the OEI to the deeper penetration of the electromagnetic field and, hence, the rf power deposition in the plasma source of our interest here. However, the comparison of the radial profiles in Fig. 13

does not reveal any substantial gain in the uniformity of the plasma density in the PSIOC compared to the ICP. We thus hope that further detailed measurements in both devices will bring in some light into this issue.

V. CONCLUSION

Electromagnetic properties of the low-frequency (0.46 MHz), inductively coupled plasma source sustained by a unidirectional oscillating internal rf current have been investigated experimentally. Spatial distribution of the electromagnetic field inside the chamber in the low-density electrostatic (E) and high-density electromagnetic (H) modes have been studied using two miniature magnetic probes. The antenna comprises two alternately reconnected sets of eight parallel current-carrying wires, in each of them the rf current flows in the same phase and direction. The original way of reconnection satisfies the principle of the minimized impedance of the entire antenna configuration, which certainly enables better efficiency of the rf power deposition into the plasma being

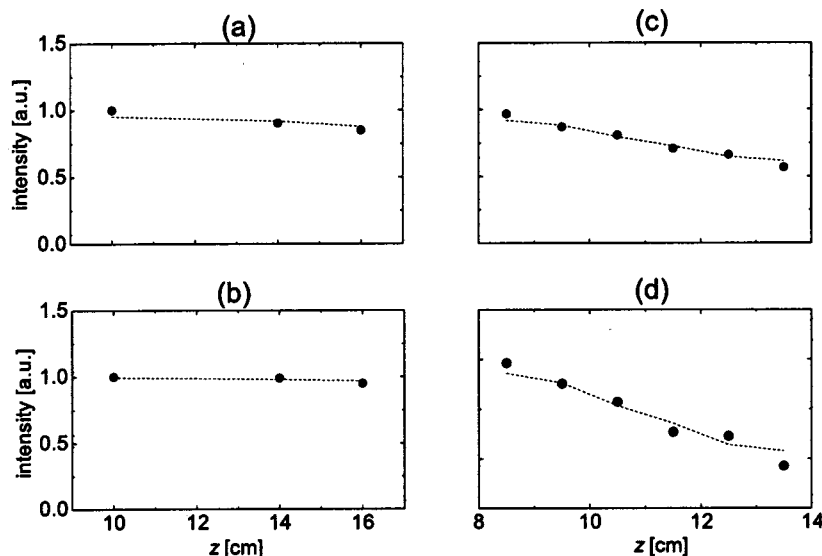


FIG. 14. Same as in Fig. 13. In diagrams (c) and (d), $P_p = 1.2$ kW and $p_0 = 40$ mTorr.

created. In addition to the three fundamental-harmonic electromagnetic field components E_ϕ , H_z , and H_r of the “pancake” coil ICPs, the originally designed antenna generates two additional fundamental frequency components, namely, H_ϕ and E_r , which results in the improvement of the uniformity of the rf power deposition as compared to conventional sources of inductively coupled plasmas with external flat spiral coils. The measured radial distributions of the magnetic fields are found in a good agreement with the numerically computed profiles. The spatially resolved profiles of the optical emission intensity indicate on the improvement of the uniformity of the plasma density over large chamber volumes.

Our ongoing work is on the quantifying the most optimal discharge control parameters when the uniformity of the rf power deposition is the best. Future work will be focused on the explanation of anomalous penetration of magnetic fields into the plasma chamber, elucidation of the possible role of nonlinear effects in the rf power deposition, and the development of self-consistent numerical models of nonuniform plasmas in low-pressure E -mode and H -mode discharges sustained by two internal crossed unidirectional current sheets.

ACKNOWLEDGMENTS

This work was supported in part by the Agency for Science, Technology, and Research of Singapore (Project No. 012 101 0024), Australian Research Council, The University of Sydney, Academic Research Fund of Nanyang Technological University, and the Lee Kuan Yew Foundation.

¹Y. J. T. Lii, in *ULSI Technology*, edited by C. Y. Chang and S. M. Sze (McGraw-Hill, New York, 1996), pp. 329–370.

²G. S. Oehrlein, *Plasma Processing of Electronic Materials* (Springer, Berlin, 2003).

³M. Meyyappan, L. Delzeit, A. Cassell, and D. Hash, *Plasma Sources Sci. Technol.* **12**, 205 (2003), and the references therein.

⁴K. Ostrikov, *Sing. J. Phys.* **19**, 1 (2003), and the references therein.

⁵H. Sugai, T. H. Ahn, I. Ghanashev, M. Goto, M. Nagatsu, K. Nakamura, K. Suzuki, and H. Toyoda, *Plasma Phys. Controlled Fusion* **39**, A445 (1997).

⁶S. V. Vladimirov and K. Ostrikov, *Phys. Rep.* **393**, 175 (2004), and the references therein.

⁷M. Tuszewski, *Phys. Plasmas* **5**, 1198 (1998).

⁸H. Sugai, K. Nakamura, and K. Suzuki, *Jpn. J. Appl. Phys., Part 1* **33**, 2189 (1994).

⁹K. Suzuki, K. Nakamura, H. Ohkubo, and H. Sugai, *Plasma Sources Sci. Technol.* **7**, 13 (1998).

¹⁰M. Tuszewski, *IEEE Trans. Plasma Sci.* **27**, 68 (1999).

¹¹I. El-Fayoumi and I. R. Jones, *Plasma Sources Sci. Technol.* **7**, 162 (1998); **7**, 179 (1998).

¹²S. Xu, K. N. Ostrikov, W. Luo, and S. Lee, *J. Vac. Sci. Technol. A* **18**, 2185 (2000).

¹³S. Xu, K. N. Ostrikov, Y. Li, E. L. Tsakadze, and I. R. Jones, *Phys. Plasmas* **8**, 2549 (2001).

¹⁴K. N. Ostrikov, I. B. Denysenko, E. L. Tsakadze, S. Xu, and R. G. Storer, *J. Appl. Phys.* **92**, 4935 (2002).

¹⁵K. Ostrikov, E. Tsakadze, S. Xu, S. V. Vladimirov, and R. Storer, *Phys. Plasmas* **10**, 1146 (2003).

¹⁶L. Stenflo and M. Y. Yu, *Nature (London)* **384**, 224 (1996).

¹⁷L. Stenflo and M. Y. Yu, *Phys. Plasmas* **5**, 3122 (1998); *Phys. Rev. A* **42**, 4894 (1990).

¹⁸C. M. Ryu and M. Y. Yu, *Phys. Scr.* **57**, 601 (1998).

¹⁹E. L. Tsakadze, K. N. Ostrikov, S. Xu, R. Storer, and H. Sugai, *J. Appl. Phys.* **91**, 1804 (2002).

²⁰J. Hopwood, C. R. Guarnieri, S. J. Whitehair, and J. J. Cuomo, *J. Vac. Sci. Technol. A* **11**, 152 (1993).

²¹K. N. Ostrikov, S. Xu, and A. B. M. Shafiul Azam, *J. Vac. Sci. Technol. A* **20**, 251 (2002).

²²Y. Wu and M. A. Lieberman, *Appl. Phys. Lett.* **72**, 777 (1998); *Plasma Sources Sci. Technol.* **9**, 210 (2000).

²³S. S. Kim, H. Y. Chang, and C. S. Chang, *Appl. Phys. Lett.* **77**, 492 (2000).

²⁴Z. Tsakadze, K. Ostrikov, S. Xu, and E. Tsakadze, *Bull. Am. Phys. Soc.* **48**, 6 (2003); **48**, 17 (2003); S. Xu, K. Ostrikov, and E. L. Tsakadze, Singapore Patent No. 1304.P014/ADR/fmy (pending); E. Tsakadze, K. Ostrikov, Z. Tsakadze, and S. Xu (unpublished).

²⁵M. A. Lieberman and A. J. Lichtenberg, *Principles of Plasma Discharges and Materials Processing* (Wiley, New York, 1994).

²⁶Y. P. Raizer, *Gas Discharge Physics* (Springer, Berlin, 1991).

²⁷J. D. Jackson, *Classical Electrodynamics* (Wiley, New York, 1975).

²⁸F. F. Chen, *Introduction to Plasma Physics and Controlled Fusion* (Plenum, New York, 1984).

²⁹A. I. Smolyakov, V. Godyak, and A. Duffy, *Phys. Plasmas* **7**, 4755 (2000).

³⁰R. B. Piejak and V. A. Godyak, *Appl. Phys. Lett.* **76**, 2188 (2000).